



Published in final edited form as:

*Mol Ther.* 2008 August ; 16(8): 1450–1458. doi:10.1038/mt.2008.127.

## Control of Endothelial Targeting and Intracellular Delivery of Therapeutic Enzymes by Modulating the Size and Shape of ICAM-1-targeted Carriers

Silvia Muro<sup>1,2,3</sup>, Carmen Garnacho<sup>1,3</sup>, Julie A Champion<sup>5</sup>, John Leferovich<sup>3</sup>, Christine Gajewski<sup>3</sup>, Edward H Schuchman<sup>4</sup>, Samir Mitragotri<sup>5</sup>, and Vladimir R Muzykantov<sup>1,2,3</sup>

<sup>1</sup> Department of Pharmacology, School of Medicine, University of Pennsylvania, Philadelphia, Pennsylvania, USA

<sup>2</sup> Institute for Translational Medicine and Therapeutics, School of Medicine, University of Pennsylvania, Philadelphia, Pennsylvania, USA

<sup>3</sup> Institute for Environmental Medicine, School of Medicine, University of Pennsylvania, Philadelphia, Pennsylvania, USA

<sup>4</sup> Department of Genetics and Genomic Sciences, Mount Sinai School of Medicine, New York, New York, USA

<sup>5</sup> Department of Chemical Engineering, College of Engineering, University of California Santa Barbara, Santa Barbara, California, USA

### Abstract

Endocytosis in endothelial cells (ECs) is important for many biomedical applications, including drug delivery by nano- and microscale carriers. However, little is known about how carrier geometry influences endothelial drug targeting, intracellular trafficking, and effects. We studied this using prototype polymer carriers of various sizes (0.1–10  $\mu\text{m}$ ) and shapes (spheres versus elliptical disks). Carriers were targeted to intercellular adhesion molecule 1 (ICAM-1), a transmembrane glycoprotein that is upregulated in many pathologies and used as a target for intraendothelial drug delivery. ECs internalized anti-ICAM-coated carriers of up to several microns in size via cell adhesion molecule-mediated endocytosis. This pathway is distinct from caveolar and clathrin endocytosis that operate for submicron-size objects. Carrier geometry was found to influence endothelial targeting in the vasculature, and the rate of endocytosis and lysosomal transport within ECs. Disks had longer half-lives in circulation and higher targeting specificity in mice, whereas spheres were endocytosed more rapidly. Micron-size carriers had prolonged residency in prelysosomal compartments, beneficial for endothelial antioxidant protection by delivered catalase. Submicron carriers trafficked to lysosomes more readily, optimizing effects of acid sphingomyelinase (ASM) enzyme replacement in a model of lysosomal storage disease. Therefore, rational design of carrier geometry will help optimize endothelium-targeted therapeutics.

## INTRODUCTION

Endothelial cells (ECs) lining the vascular lumen represent an important target for therapeutic interventions in numerous acute and chronic diseases.<sup>1–4</sup> Optimizing targeted delivery of therapeutics to vascular ECs is, therefore, an important medical goal.<sup>2–8</sup> However, most therapeutics do not have intrinsic affinity to ECs (or other cell types).<sup>1–3</sup> This results in rapid clearance from the blood and inefficient transport into endothelium, leading to suboptimal delivery and effects.<sup>1–3</sup>

In theory, this obstacle can be surmounted by coupling drugs of interest to targeting vectors (*e.g.*, antibodies) that recognize determinants expressed on the endothelial surface at sites of disease.<sup>2,3,5–7,9,10</sup> For example, intercellular adhesion molecule 1 (ICAM-1) is a leukocyte anchor expressed primarily in the luminal surface of ECs.<sup>11,12</sup> This molecule is upregulated and functionally involved in many disease conditions including inflammation, oxidative stress, atherosclerosis, thrombosis, and metabolic disorders.<sup>11,12</sup> Hence, ICAM-1 represents a candidate determinant for endothelial targeting of drugs designed for treatment of these pathologies.<sup>2,6,13</sup> ICAM-1 targeting by anti-ICAM antibodies or antibody fragments facilitates vascular delivery of imaging agents,<sup>14,15</sup> immunoliposomes,<sup>13</sup> therapeutics, and reporter agents to resting and pathologically activated endothelium.<sup>6,16–21</sup> Therefore, understanding the mechanisms regulating endothelial drug delivery via ICAM-1 is an important goal.

Interestingly, ECs do not internalize ICAM-1 antibodies, but internalize multivalent anti-ICAM conjugates and anti-ICAM-coated polymer nanocarriers.<sup>16,17,19</sup> These multivalent formulations induce ICAM-1 clustering and endocytosis via a unique pathway, cell adhesion molecule (CAM)-mediated endocytosis.<sup>17,22</sup> CAM-endocytosis is independent from clathrin-, caveolar-, macropinocytosis- and phagocytosis-mediated pathways.<sup>17,22</sup>

CAM-endocytosis induced by conjugates and nanocarriers targeted to EC adhesion molecules provides intracellular delivery of therapeutics. This is the case for catalase that protects against vascular oxidative stress in cells and animal models.<sup>18,23,24</sup> Following internalization, anti-ICAM carriers traffic to lysosomes, where proteolysis terminates the therapeutic effect of catalase.<sup>18,25</sup> However, in an alternative therapeutic application, lysosomes represent an ideal destination of anti-ICAM carriers loaded with enzymes for replacement therapies for lysosomal storage disorders.<sup>20,21,26</sup>

Previous studies of endothelial drug transport via ICAM-1 used spherical anti-ICAM carriers with diameters 0.1–0.2  $\mu\text{m}$ .<sup>17–20,22,25</sup> Intuitively, one can expect that the size and shape of a drug carrier can modulate its circulation in the blood, distribution in organs, endothelial uptake, intracellular transport, and fate. Previous *in vitro* studies in macrophages lend indirect support to this notion: macrophages internalize immunoglobulin G (IgG)-coated polystyrene spheres with diameters of 0.2  $\mu\text{m}$  versus 2  $\mu\text{m}$  with similar kinetics.<sup>27</sup> However, different pathways are involved in the uptake of these particles (clathrin endocytosis versus classical phagocytosis, respectively).<sup>27</sup> As a result, micron particles traffic to lysosomes in macrophages faster than their submicron counterparts.<sup>27</sup> The shape of micron-size polystyrene particles also modulates the rate of phagocytosis by macrophages.<sup>28</sup> However, the role of carrier geometry in endothelial transport has not been previously studied and may be different from that observed in macrophages. In general, the role of carrier geometry in targeted drug delivery remains unclear.

In order to fill this gap, we designed prototype anti-ICAM carriers of diverse shape (polystyrene spheres versus elliptical disks) and size (mean diameters ranging from 0.1 to 10  $\mu\text{m}$ ). Blood circulation and endothelial targeting of these carriers was tested in mice. Carrier endocytosis, trafficking, and intracellular fate were evaluated in ECs in culture. The results permitted us to identify anti-ICAM carriers with geometries optimized for intracellular delivery of antioxidant enzymes versus lysosomal enzyme replacement therapies. The therapeutic effects of these

carriers were tested in experimental cell models for vascular protection against oxidative stress and treatment of lysosomal storage disorders, respectively.

## RESULTS

### The geometry of anti-ICAM carriers controls their clearance from the circulation and endothelial targeting in the vasculature

The biodistribution of radiolabeled anti-ICAM carriers of various geometries, including spheres (0.1, 1, 5, and 10  $\mu\text{m}$  diameter) and elliptical disks ( $0.1 \times 1 \times 3 \mu\text{m}$ ), was quantified after intravenous injection in mice (Figure 1). We focused on the liver, which represents the main site for “nonspecific” uptake of circulating particles by the reticuloendothelial system, and the pulmonary vasculature, which represents a favorable site for endothelial targeting because it contains ~30% of the total endothelial surface in the body and receives 100% cardiac venous output.<sup>2</sup>

In agreement with our previous studies,<sup>19</sup> submicron-size (0.1  $\mu\text{m}$  diameter) anti-ICAM spheres showed rapid clearance from the blood:  $16.2 \pm 2.7\%$  of the injected dose (% ID) and  $5.2 \pm 0.5\%$  ID at 1 minute and 30 minutes after injection, respectively (Figure 1a). This was, at least in part, due to hepatic uptake of these carriers:  $43.7 \pm 4.5\%$  of the ID per gram of organ (% ID/g; Figure 1b). Most importantly, these ICAM-1-targeted carriers showed efficient and specific pulmonary uptake versus control IgG spheres:  $114.7 \pm 11.1\%$  ID/g versus  $10.2 \pm 3.9\%$  ID/g, respectively (Figure 1c). The pulmonary immunospecificity index of submicron-size anti-ICAM carriers (ISI, which represents the ratio of % ID/g of anti-ICAM to IgG carriers) was 11.3, indicating robust endothelial targeting (Figure 1d).

Larger 1, 5, and 10  $\mu\text{m}$  anti-ICAM spheres were cleared from the circulation even faster than their 0.1  $\mu\text{m}$  counterparts:  $13.0 \pm 1.1\%$  ID,  $8.7 \pm 0.2\%$  ID, and  $7.1 \pm 2.8\%$  ID remained in the blood 1 minute after injection (Figure 1a). Rapid blood clearance occurred despite the fact that hepatic uptake of these micron-range anti-ICAM carriers was lower:  $22.5 \pm 1.8\%$  ID/g,  $7.2 \pm 0.4\%$  ID/g, and  $5.6 \pm 0.7\%$  ID/g (Figure 1b). This can be explained in part by even more profound pulmonary uptake, exceeding that of 0.1  $\mu\text{m}$  spheres:  $158.0 \pm 19.0\%$  ID/g,  $235.1 \pm 14.6\%$  ID/g, and  $219.0 \pm 51.2\%$  ID/g for 1, 5, and 10  $\mu\text{m}$  anti-ICAM spheres (Figure 1c). Notably, control IgG spheres of 1, 5, and 10  $\mu\text{m}$  in diameter also displayed high pulmonary uptake:  $99.2 \pm 11.3\%$  ID/g,  $153.1 \pm 5.8\%$  ID/g, and  $133.5 \pm 7.3\%$  ID/g (Figure 1c), which is in contrast to the submicron spheres. Thus, the pulmonary immunospecificity index was ~1.6 for spheres that were larger than a micron in diameter, revealing a dominant role of nonspecific mechanical retention of micron-size spheres in pulmonary capillaries (Figure 1d).

We next examined the role of particle shape on the blood clearance rate and uptake. Anti-ICAM disks ( $0.1 \times 1 \times 3 \mu\text{m}$ ) remained in the circulation for longer periods of time than their spherical counterparts:  $25.5 \pm 2.8\%$  ID and  $20.9 \pm 1.6\%$  ID remained in the blood at 1 and 30 minutes after injection, respectively (Figure 1a). They also showed lower uptake by the liver ( $15.7 \pm 2.3\%$  ID/g; Figure 1b) and very specific targeting to the lungs ( $186.2 \pm 15.4\%$  ID/g versus  $5.2 \pm 0.5\%$  ID/g for IgG disks; Figure 1c). As a result, anti-ICAM disks had the highest pulmonary anti-ICAM-to-IgG immunospecificity index value of 35.7 (Figure 1d). Therefore, both submicron-size spheres and elliptical disks provide favorable geometries to design carriers for ICAM-1-directed endothelial targeting, particularly to the lung.

Analysis of lung tissue by transmission electron microscopy 3 hours after injection of carriers further revealed that both 0.1- $\mu\text{m}$  anti-ICAM spheres and  $0.1 \times 1 \times 3 \mu\text{m}$  anti-ICAM disks resided within vesicular compartments inside pulmonary endothelium, with no detectable signs of cell damage, disruption of endothelial junctions, pulmonary edema, or other signs of lung injury (Figure 2). To the best of our knowledge, this is the first evidence of *in vivo*

intraendothelial targeting of polymer carriers with dimensions that exceed the typical size of clathrin pits and caveolar vesicles (which usually accommodate intracellular transport of submicron ligands<sup>29,30</sup>).

### The effects of geometry on the internalization of anti-ICAM carriers by ECs

We next explored the role of the geometry of anti-ICAM carriers on their internalization by ECs. For these studies, we used cell cultures of human umbilical vein ECs (activated with tumor necrosis factor- $\alpha$  to enhance the expression of ICAM-1), as in our previous work.<sup>17,22</sup> Fluorescently labeled anti-ICAM spheres and elliptical disks, but not their IgG counterparts, bound specifically to ECs in culture (Figure 3). Double-label fluorescence microscopy analysis (Figure 4a) showed that the ECs endocytosed 5- $\mu\text{m}$  anti-ICAM spheres as rapidly as 0.1- $\mu\text{m}$  spheres:  $81.4 \pm 2.8\%$  and  $94.2 \pm 2.9\%$  internalization at 1 hour ( $t_{1/2} \sim 15$  minutes in both cases). Anti-ICAM disks ( $0.1 \times 1 \times 3 \mu\text{m}$ ) were also internalized by ECs in culture (Figure 4). However, the internalization kinetics of disks was markedly slower ( $t_{1/2} \sim 1$  hour; Figure 4) than that of spherical anti-ICAM carriers despite the fact that, even in their maximal dimension, the disks were smaller than 5- $\mu\text{m}$  spheres.

### ECs internalize anti-ICAM carriers of diverse geometries via CAM-mediated endocytic pathway associated with formation of actin stress fibers

Delayed endocytosis of anti-ICAM disks versus spheres could be due to involvement of a different endocytic mechanism or/and different reorganization of the cytoskeleton, necessary to facilitate plasma membrane deformation and invagination during endocytosis. To explore this, we imaged actin filaments using phalloidin and fluorescence microscopy in cells incubated with either anti-ICAM spheres (0.5  $\mu\text{m}$  versus 5  $\mu\text{m}$ ) or disks (Figure 5a). We observed that, regardless of their size and progression of internalization, binding of anti-ICAM spheres and disks to ECs resulted in rapid reorganization of the actin cytoskeleton into bundles of stress fibers (Figure 5a). Actin fibers aligned beneath the particles, similar to actin remodeling by 0.1–0.2- $\mu\text{m}$  anti-ICAM spheres tested previously.<sup>17,22</sup> Interestingly, concomitant to their internalization, we observed a delayed and progressive alignment of anti-ICAM disks in the orientation of the actin bundles (Figure 5a).

We then determined whether a different endocytic pathway accounts for the differences observed in the actin alignment and internalization rate of anti-ICAM carriers of different geometries (0.1-, 1-, and 5- $\mu\text{m}$  diameter spheres versus  $0.1 \times 1 \times 3 \mu\text{m}$  elliptical disks). Treatment with pharmacological inhibitors showed that all tested anti-ICAM carriers were internalized by ECs via a similar pathway (Figure 5b and c). Cytochalasin D, which caps short actin filaments, did not affect internalization of anti-ICAM spheres or disks (Figure 5b). In contrast, uptake of both anti-ICAM carriers was inhibited by latrunculin A, a more potent actin depolymerizing agent (Figure 5b). This result is in agreement with our previous data showing endocytosis of anti-ICAM carriers (0.1  $\mu\text{m}$  diameter) via an actin-dependent, yet nonclassical, endocytic mechanism.<sup>17</sup> Confirming this, endocytosis of the anti-ICAM carriers was distinct from endocytosis mediated by clathrin-coated pits (inhibited by monodansyl cadaverine), caveoli (inhibited by filipin), or macropinocytosis (inhibited by amiloride and wortmannin) (Figure 5c). Instead, all anti-ICAM carriers were internalized by the CAM-mediated pathway, which is affected by amiloride, but not wortmannin (Figure 5c).

### The size of anti-ICAM carriers controls their intracellular trafficking in ECs

We used a multi-label fluorescence microscopy approach established previously<sup>18</sup> to study how the geometry of anti-ICAM carriers affects their intracellular trafficking (Figure 6) and the stability of their protein coat after internalization (Figure 7). In agreement with our previous studies,<sup>18,25</sup> the majority ( $71.8 \pm 0.5\%$ ) of 0.1- $\mu\text{m}$  anti-ICAM spheres internalized by ECs trafficked to lysosomes by 3 hours (Figure 6). In contrast, even at 5 hours after endocytosis, a

significantly smaller fraction of micron-size anti-ICAM carriers was located within lysosomes (~25–30% reduction), regardless of the carrier spherical or elliptical disks shape (Figure 6). Apparently, intracellular transport of micron-size anti-ICAM carriers reached saturation ~2 hours after their internalization (Figure 6).

In addition, the protein coat of the carriers (anti-ICAM absorbed on the polymer surface) was degraded in accordance with the trafficking to lysosomes (Figure 7). Degradation was practically complete by 3 hours in the case of 0.1- $\mu\text{m}$  anti-ICAM spheres (Figure 7). In contrast, micron-size anti-ICAM spheres or disks retained ~30% of protein coat even at 5 hours after internalization (Figure 7). This result is in agreement with the prolonged residence of micron-size range carriers in prelysosomal compartments (Figure 6).

### **Design of anti-ICAM carrier geometry for selected cargoes: optimization of the intracellular destination and effects of distinct therapeutic proteins**

The results described earlier may guide the design of more effective carriers for intracellular drug delivery via ICAM-1. The distinct targeting, endocytosis, and intracellular transport properties of anti-ICAM carriers of different sizes and shapes provide variable drug delivery opportunities, adjustable to specific therapeutic needs.

We tested this possibility using anti-ICAM carriers coated with two experimental therapeutic enzymes which require different subcellular destinations. The first enzyme is catalase, an  $\text{H}_2\text{O}_2$ -degrading antioxidant enzyme. Targeting catalase into ECs via cell adhesion molecules protects endothelium against vascular oxidative stress *in vitro* and *in vivo*.<sup>23</sup> However, trafficking to lysosomes leads to catalase degradation and limits the duration of its protective effect.<sup>18,22,25</sup> The second enzyme is acid sphingomyelinase (ASM), a lysosomal enzyme deficient in types A and B Niemann–Pick disease, an inherited disorder characterized by lysosomal accumulation of sphingomyelin.<sup>31</sup> This lipid storage can be alleviated by lysosomal delivery of enzyme replacement therapies.<sup>20,21,32</sup>

As shown in a Figure 8a, submicron-size anti-ICAM/catalase carriers protected ECs from  $\text{H}_2\text{O}_2$  oxidative injury. However, antioxidant protection lasted for <3 hours after internalization, due to lysosomal proteolysis of catalase as we observed previously.<sup>23,25</sup> In contrast, catalase delivered into ECs using micron-size anti-ICAM carriers provided total protection against the same oxidative insult for at least 5 hours after internalization (the duration of the study; Figure 8a). This prolonged protection is likely due to limited lysosomal delivery of micron-size anti-ICAM carriers (see Figure 6). In contrast, and likely by the same reason, delivery of ASM loaded onto micron-size anti-ICAM spheres provided only partial attenuation of abnormal sphingomyelin storage in imipramine-treated HUVECs, a pharmacological model of ASM-deficient Niemann–Pick disease (Figure 8b). However, excess sphingomyelin was completely degraded by ASM delivered by submicron-size anti-ICAM carriers (Figure 8b), which traffic efficiently to lysosomes, the intended target for this therapeutic.<sup>20,32</sup> Thus, optimization of the geometry of anti-ICAM carriers helps to customize their use for diverse therapeutic needs, each of which has specific requirements in terms of the desired subcellular localization and effect.

## **DISCUSSION**

In this work, we show that endothelial targeting and intracellular destination of model polymer carriers targeted to ICAM-1 can be modulated by carrier geometry, in particular the size and shape. Micron-size anti-ICAM spheres accumulate nonspecifically in the pulmonary vasculature after intravenous injection, likely due to mechanical entrapment of these particles in small capillaries (Figure 1). Submicron anti-ICAM spheres show rapid and specific pulmonary uptake, reflecting endothelial targeting (Figure 1). In contrast, micron-size anti-

ICAM elliptical disks had a prolonged half-life in the circulation and specific endothelial targeting (Figure 1). It is tempting to speculate that hydrodynamic features of elliptical disks in the bloodstream, such as alignment with flow, may prolong disk half-life in circulation by diminishing nonspecific collisions with the vascular walls. This paradigm is illustrated in biology by long-circulating discoid red blood cells circulating in the blood, and also by recent findings implying that elongated liposomes and polymer filomicelles circulate for a prolonged time period due to flow alignment.<sup>33,34</sup> In addition, the higher surface-to-volume ratio of micron-size elliptical disks versus spheres may diminish the detaching forces acting on endothelium-anchored anti-ICAM disks in the bloodstream.

Both anti-ICAM submicron spheres and micron-size disks are internalized by pulmonary ECs *in vivo* (Figure 2), showing an impressive capacity of anti-ICAM carriers to target and enter ECs. Thus, targeting features of ICAM-1 markedly differ from those of determinants associated with classical endocytic pathways restricted to much smaller objects. For example, ~1- $\mu$ m phage particles expressing a peptide with high affinity to a lung endothelial, caveolae-specific protein neither bind to endothelium, nor enter caveoli *in vivo*.<sup>35</sup> This is due to size restriction of caveolar invaginations, because both the free peptide and an antibody to this protein could bind to endothelium, accumulate in lungs, and enter caveoli.<sup>35</sup>

At the cellular level, spheres seem to be the most permissive shape for endocytosis of anti-ICAM carriers ranging from 0.1 to 5  $\mu$ m (Figure 4). In contrast, uptake of large anti-ICAM elliptical disks is delayed (Figure 4). Slow transport of anti-ICAM disks may be due to higher surface-to-volume ratio of disks versus spheres, given that this parameter dictates the need for higher plasmalemma deformability to adapt to disks, which have more pronounced and varying curvature. A similar phenomenon was recently observed for phagocytosis of IgG-opsonized particles by macrophages, which was governed by formation and progression of actin cups beneath the plasma membrane.<sup>28</sup> However, in contrast with phagocyte uptake of IgG-opsonized particles, anti-ICAM carriers did not elicit actin polymerization into cups around spherical or disk particles, regardless of anti-ICAM carrier geometry and the progression of internalization (Figure 5a). Instead, anti-ICAM carriers induced formation of actin stress fibers (Figure 5a and refs. <sup>17,22</sup>) and their endocytosis was inhibited by the actin filament inhibitor latrunculin A, but not by cytochalasin D that typically affects classical actin-dependent endocytosis (Figure 5b). A similar reorganization of the actin cytoskeleton has been previously observed for 0.1–0.2- $\mu$ m diameter anti-ICAM spheres, which is mediated by RhoA activation and ROCK signaling.<sup>17,36</sup> This suggests that endocytosis of anti-ICAM carriers with different geometries operates via a similar, nonclassical uptake pathway.<sup>17</sup>

Indeed, regardless of anti-ICAM carrier geometry, internalization occurs via CAM-mediated endocytosis (Figure 5c and ref. <sup>17</sup>), which bypasses classical endothelial mechanisms of endocytosis, such as caveolar-<sup>37</sup> and clathrin-mediated pathways.<sup>30</sup> CAM-endocytosis permits uptake of particles up to several microns in size (Figure 4b, also confirmed *in vivo* in Figure 2). This is in contrast to a previous report showing that cells switched from clathrin- to caveolar-mediated pathways with increasing particle size.<sup>38</sup> However, the cells used in that study were not endothelial, and the polystyrene particles were not targeted to any specific cellular receptor, implicating less specific and passive uptake mechanisms. Internalization of anti-ICAM carriers depends on amiloride-sensitive NHE1.<sup>17,22</sup> This is an ion exchanger that interacts with ICAM-1 engaged by anti-ICAM carriers and acts as a crosslinker of actin filaments, likely through binding of its cytosolic tail to ezrin-radixin-moesin family proteins.<sup>22</sup> NHE1 regulates the apical surface elasticity of endothelium,<sup>39</sup> which may explain the high permissibility of CAM-endocytosis for particulate ligands of variable size and shape.

In contrast to endocytosis, mainly ruled by carrier shape (Figure 4), intracellular transport of internalized anti-ICAM carriers to lysosomes is controlled by carrier size. Submicron-size anti-

ICAM carriers show more efficient transport to lysosomes, with concomitant degradation of the protein coat (Figures 6 and 7). Micron-size anti-ICAM spheres or disks reside protected within prelysosomal compartments for longer periods of time (Figures 6 and 7). This is unlike lysosomal trafficking of IgG-opsonized particles by macrophages, which increases with increasing particle size.<sup>27</sup> Perhaps less effective lysosomal trafficking of micron-size anti-ICAM carriers by ECs may reflect more restrictive dimensions of intracellular vesicular machinery within this cell type.

Regarding the intracellular fate of the carriers, it should be noted that polystyrene particles used in this study are not degradable and reside within vesicular compartments in ECs for prolonged periods of time. However, they represent a good model carrier as these particles show the same targeting and intracellular transport features as carriers formulated from biocompatible US Food and Drug Administration–approved poly(lactic co-glycolic) acid.<sup>19, 21</sup> For instance, our recent studies in cell culture and animal models indicate that polystyrene and poly(lactic co-glycolic) acid nanocarriers targeted to ICAM-1 provide very similar results regarding intracellular delivery of recombinant ASM in vascular endothelium.<sup>21</sup> Poly(lactic co-glycolic) acid represents a highly promising formulation for future translational studies on ICAM-1-targeted delivery, as it is a safe polymer that can be metabolized in tissues and displays low toxic and immunogenic effects.<sup>40–42</sup>

Prelysosomal versus lysosomal transport of anti-ICAM carriers, regulated by modulating carrier size, highlights the variability and potential utility of the ICAM-1-targeting platform for therapeutic applications that require distinct intracellular localization and duration of effects. As an example with relevant implications in the design of endothelial antioxidant therapies, we have used micron-size anti-ICAM carriers and have shown ICAM-1-mediated delivery and prolonged antioxidant protection by catalase in prelysosomal compartments (Figure 8a). In addition, as a distinct example relevant to the treatment of lysosomal storage disorders, we have used submicron-size anti-ICAM carriers to deliver recombinant ASM to endothelial lysosomes for attenuation of accumulated sphingomyelin (Figure 8b).

In conclusion, the size and shape of anti-ICAM carrier particles (and, perhaps, carriers targeted to other surface determinants) can be tuned to control the pharmacokinetics and biodistribution of these carriers *in vivo*, as well as the intracellular delivery and effects of therapeutic cargoes. These parameters can be designed to better fit the needs of particular therapeutic approaches.

## MATERIALS AND METHODS

### Antibodies and reagents

Monoclonal antibodies to human and mouse ICAM-1 were mAb R6.5 and YN1, respectively.<sup>19</sup> Fluorescent secondary antibodies, dextran, phalloidin, BODIPY-Fl<sub>C12</sub>-sphingomyelin, and the Live/Dead kit were from molecular Probes (Eugene, OR). Fluorescein isothiocyanate polystyrene microspheres (0.1, 0.5, 1, 5, and 10  $\mu\text{m}$  diameter) were from Polysciences (Warrington, PA). Elliptical disks (0.1  $\times$  1  $\times$  3  $\mu\text{m}$ ) were prepared from uncrosslinked 2- $\mu\text{m}$  diameter polystyrene spheres as described previously.<sup>28</sup> Recombinant human ASM was produced in Chinese hamster ovary cells and purified as described previously.<sup>32</sup> Unless specified otherwise, all other reagents were from Sigma (St Louis, MO).

### Anti-ICAM carriers of various geometries

Anti-ICAM versus control IgG spheres or disks were prepared by absorption of anti-ICAM or nonspecific IgG onto fluorescein isothiocyanate polystyrene particles.<sup>18</sup> For experiments *in vivo*, radiolabeled particles contained a mix of either anti-ICAM or IgG and <sup>125</sup>I-IgG at 95:5 molar ratio.<sup>18</sup> Catalase or ASM were coadsorbed with anti-ICAM onto polystyrene carriers as

described previously.<sup>18,20</sup> The final diameter of the carriers was determined by dynamic light scattering.

### **Biodistribution of anti-ICAM carriers in mice**

Anesthetized C57Bl/6 male mice were injected intravenously with <sup>125</sup>I-labeled anti-ICAM or control IgG carriers (~1.3 mg IgG and  $5.6 \times 10^{11}$   $\mu\text{m}^2$  total particle surface per kg of body weight). Blood samples were collected from the retro-orbital plexus at 1 and 30 minutes after injection, and organs (kidneys, heart, spleen, liver, and lungs) were collected 30 minutes after injection. The percent of the total injected dose (% ID), percent ID per gram of organ (% ID/g), organ-to-blood localization ratio (% ID/g in an organ: % ID/g in blood), and anti-ICAM-to-IgG immunospecificity index (% ID/g in a tissue for targeted versus nontargeted formulations) were determined as described previously.<sup>19</sup>

Alternatively, anti-ICAM carriers were imaged by transmission electron microscopy. For this purpose, mice injected with nonradiolabeled carriers were perfused 3 hours after injection first with phosphate-buffered saline and then with fixative (2.5% glutaraldehyde, 4% paraformaldehyde in 0.1 mol/l Na cacodylate buffer). Perfusions were done through the left ventricle while animals were maintained under ventilation. Lung samples were collected and processed from 80-nm thin resin-embedded sections (Biomedical Imaging Facility, University of Pennsylvania, Philadelphia, PA).

All animal studies were performed in accordance with the Guide for the Care and Use of Laboratory Animals as adopted by the US National Institutes of Health, and all protocols were approved by the University of Pennsylvania.

### **Actin remodeling and endocytosis of anti-ICAM carriers in cell culture**

Human umbilical vein ECs or HUVECs (Clonetics, San Diego, CA) were seeded onto gelatin-coated coverslips in 24-well plates and grown in supplemented M199 medium (GibcoBRL, Grand Island, NY). Cells were treated overnight with 10 ng/ml tumor necrosis factor- $\alpha$  to stimulate ICAM-1 expression.<sup>17</sup> Fluorescein isothiocyanate-labeled anti-ICAM or control IgG carriers were first incubated with HUVECs for 30 minutes at 4 °C to permit binding. Then, nonbound carriers were washed and the cells were warmed at 37 °C to permit endocytosis, either in the absence or presence of pharmacological inhibitors of endocytosis pathways (50  $\mu\text{mol/l}$  monodansyl cadaverine, 1  $\mu\text{g/ml}$  filipin, 3 mmol/l amiloride, or 0.5  $\mu\text{mol/l}$  wortmannin) or inhibitors of actin filaments (0.5  $\mu\text{mol/l}$  cytochalasin D or 0.1  $\mu\text{mol/l}$  latrunculin A). The cells were washed in the cold, fixed with 2% paraformaldehyde, and surface-bound carriers were stained with goat anti-mouse IgG conjugated to Texas red.<sup>17</sup> The samples were analyzed with a Nikon Eclipse TE2000-U fluorescence microscope (Nikon, Melville, NY), using a 40 $\times$  PlanApo objective and filters optimized for fluorescein isothiocyanate and Texas red fluorescence. Images were obtained with a Hamamatsu Orca-1 charge-coupled device camera and analyzed using ImagePro 3.0 software (Media Cybernetics, Silver Spring, MD). With this protocol, carriers bound to the cell surface are double-labeled (yellow particles) in merged fluorescence images, whereas single-labeled green particles represent internalized carriers.

Alternatively, cells were incubated in the presence of anti-ICAM carriers for various periods of time at 37 °C, following by cell fixation in cold. The samples were then permeabilized with 0.2% Triton X-100, and staining with phalloidin conjugated to red Alexa Fluor 594 to selectively stain filamentous actin.<sup>17</sup>

### **Trafficking and stability of anti-ICAM carriers**

HUVEC lysosomes were labeled with Texas red dextran (10,000 MW) and the cells were incubated with green-fluorescent anti-ICAM carriers as described earlier. The samples were

imaged using the microscope system described earlier after labeling noninternalized carriers with blue Alexa Fluor 350 goat antimouse IgG.<sup>18</sup> Surface blue-positive carriers were subtracted from tri-color images to focus on internalized counterparts. These corrected images were used to quantify the percent of green-labeled carriers colocalizing with red-labeled lysosomes with respect to the total amount of carriers internalized per cell.<sup>18</sup>

To determine the intracellular stability of the antibody component of green-fluorescent anti-ICAM carriers, fixed cells were first stained with blue Alexa Fluor 350 goat anti-mouse IgG to label surface located carriers. Cells were then permeabilized and the internalized carriers were counterstained with Texas red goat anti-mouse IgG, which recognizes nondegraded anti-ICAM on the coat of the carriers.<sup>18</sup> Surface blue-positive carriers were subtracted from tri-color micrographs and the fraction of internalized green-labeled carriers presenting “stable” red-labeled anti-ICAM coating was quantified.<sup>18</sup>

### Antioxidant protection by anti-ICAM/catalase carriers

The antioxidant effect of anti-ICAM/catalase carriers was tested after their internalization in HUVECs. For this purpose, the cells were incubated for 15 minutes at room temperature with 5 mmol/l H<sub>2</sub>O<sub>2</sub> in phenol red-free Rosewell Park Memorial Institute medium. HUVECs were then washed, incubated with Live/Dead kit containing 0.1 mmol/l calcein AM and 1 mmol/l ethidium for 15 minutes at 37 °C, and scored as percentage of calcein positive/ethidium negative, surviving cells.<sup>25</sup>

### Functional activity of anti-ICAM/ASM carriers

HUVECs were treated with 50 µmol/l imipramine overnight to induce pharmacological inhibition of endogenous ASM as described previously.<sup>20</sup> Concomitantly, the cells were incubated with fluorescent BODIPY-FL<sub>C12</sub>-sphingomyelin, which fluoresces at 620 nm (red) at high concentrations, to image intracellular (lysosomal) accumulation of sphingomyelin by fluorescence microscopy. Cells were subsequently treated either with control media or media containing submicron (0.1 µm) versus micron-size (1 µm) anti-ICAM/ASM carriers for 30 minutes at 37 °C. Cells were washed, incubated with control media for 3 hours, and finally analyzed by fluorescence microscopy to determine whether the delivered enzyme reverts lysosomal accumulation of sphingomyelin.<sup>20</sup>

### Statistics

Unless otherwise stated, the data were calculated as the mean ± SE of the mean (mean ± SEM), where statistical significance was determined by Student's *t*-test.

### Acknowledgments

We thank Michael Koval (Emory University, Atlanta, GA) for his guidance on endocytosis and trafficking of anti-ICAM carriers, and Qian-Chun Yu and Neelima Shah (Biomedical Imaging Core, University of Pennsylvania, Philadelphia, PA) for technical help with transmission electron microscopy. This study was funded by American Heart Association 0435181N, NIH R21 HL85533, and NIH-UPenn Pilot Grant P30 DK47757-14 (to S. Muro), NIH NHLBI-PEN (to S. Mitragotri), NIH R01 HD28607 (to E.S.), NIH R01 HL080396, NIH P01 HL079063, and UPenn-ITMAT Pilot Grant (to V.M.). The authors declare no competing financial interests.

### References

1. Song BW, Vinters HV, Wu D, Pardridge WM. Enhanced neuroprotective effects of basic fibroblast growth factor in regional brain ischemia after conjugation to a blood-brain barrier delivery vector. *J Pharmacol Exp Ther* 2002;301:605–610. [PubMed: 11961063]
2. Muzykantov V. Targeting drugs to pulmonary endothelium. *Expert Opinion Drug Delivery* 2005;2:909–926.

3. Oh P, Li Y, Yu J, Durr E, Krasinska KM, Carver LA, et al. Subtractive proteomic mapping of the endothelial surface in lung and solid tumours for tissue-specific therapy. *Nature* 2004;429:629–635. [PubMed: 15190345]
4. Wilson A, He F, Li J, Ma Z, Pitt B, Li S. Targeted delivery of therapeutic oligonucleotides to pulmonary circulation. *Adv Genet* 2005;54:21–41. [PubMed: 16096006]
5. Molema G. Tumor vasculature directed drug targeting: applying new technologies and knowledge to the development of clinically relevant therapies. *Pharm Res* 2002;19:1251–1258. [PubMed: 12403059]
6. Ding BS, Dziubla T, Shuvaev VV, Muro S, Muzykantov VR. Advanced drug delivery systems that target the vascular endothelium. *Mol Interv* 2006;6:98–112. [PubMed: 16565472]
7. McIntosh DP, Tan XY, Oh P, Schnitzer JE. Targeting endothelium and its dynamic caveolae for tissue-specific transcytosis *in vivo*: a pathway to overcome cell barriers to drug and gene delivery. *Proc Natl Acad Sci USA* 2002;99:1996–2001. [PubMed: 11854497]
8. Wilson A, Zhou W, Champion HC, Alber S, Tang ZL, Kennel S, et al. Targeted delivery of oligodeoxynucleotides to mouse lung endothelial cells *in vitro* and *in vivo*. *Mol Ther* 2005;12:510–518. [PubMed: 15953766]
9. Nowak K, Weih S, Metzger R, Albrecht RF 2nd, Post S, Hohenberger P, et al. Immunotargeting of catalase to lung endothelium via anti-angiotensin-converting enzyme antibodies attenuates ischemia-reperfusion injury of the lung *in vivo*. *Am J Physiol Lung Cell Mol Physiol* 2007;293:L162–L169. [PubMed: 17435080]
10. Sakhalkar HS, Hanes J, Fu J, Benavides U, Malgor R, Borroso CL, et al. Enhanced adhesion of ligand-conjugated biodegradable particles to colitic venules. *FASEB J* 2005;19:792–794. [PubMed: 15764649]
11. Muro, S. Intercellular adhesion molecule-1 and vascular cell adhesion molecule-1. In: Aird, WC., editor. *Endothelial Biomedicine*. Vol. 1. Cambridge Univ. Press; New York: 2007. p. 1058–1070.
12. Marlin SD, Springer TA. Purified intercellular adhesion molecule-1 (ICAM-1) is a ligand for lymphocyte function-associated antigen 1 (LFA-1). *Cell* 1987;51:813–819. [PubMed: 3315233]
13. Bloemen PG, Henricks PA, van Bloois L, van den Tweel MC, Bloem AC, Nijkamp FP, et al. Adhesion molecules: a new target for immunoliposome-mediated drug delivery. *FEBS Lett* 1995;357:140–144. [PubMed: 7805880]
14. Villanueva FS, Jankowski RJ, Klivanov S, Pina ML, Alber SM, Watkins CS, et al. Microbubbles targeted to intercellular adhesion molecule-1 bind to activated coronary artery endothelial cells. *Circulation* 1998;98:1–5. [PubMed: 9665051]
15. Weiner RE, Sasso DE, Gionfriddo MA, Thrall RS, Syrbu S, Smilowitz HM, et al. Early detection of oleic acid-induced lung injury in rats using (111)In-labeled anti-rat intercellular adhesion molecule-1. *J Nucl Med* 2001;42:1109–1115. [PubMed: 11438635]
16. Murciano JC, Muro S, Koniaris L, Christofidou-Solomidou M, Harshaw DW, Albelda SM, et al. ICAM-directed vascular immunotargeting of antithrombotic agents to the endothelial luminal surface. *Blood* 2003;101:3977–3984. [PubMed: 12531816]
17. Muro S, Wiewrodt R, Thomas A, Koniaris L, Albelda SM, Muzykantov VR, et al. A novel endocytic pathway induced by clustering endothelial ICAM-1 or PECAM-1. *J Cell Sci* 2003;116:1599–1609. [PubMed: 12640043]
18. Muro S, Gajewski C, Koval M, Muzykantov VR. ICAM-1 recycling in endothelial cells: a novel pathway for sustained intracellular delivery and prolonged effects of drugs. *Blood* 2005;105:650–658. [PubMed: 15367437]
19. Muro S, Dziubla T, Qiu W, Leferovich J, Cui X, Berk E, et al. Endothelial targeting of high-affinity multivalent polymer nanocarriers directed to intercellular adhesion molecule 1. *J Pharmacol Exp Ther* 2006;317:1161–1169. [PubMed: 16505161]
20. Muro S, Schuchman EH, Muzykantov VR. Lysosomal enzyme delivery by ICAM-1-targeted nanocarriers bypassing glycosylation- and clathrin-dependent endocytosis. *Mol Ther* 2006;13:135–141. [PubMed: 16153895]
21. Garnacho C, Dhimi R, Simone E, Dziubla T, Leferovich J, Schuchman EH, et al. Delivery of acid sphingomyelinase in normal and Niemann-Pick disease mice using ICAM-1-targeted polymer nanocarriers. *J Pharmacol Exp Ther* 2008;325:400–408. [PubMed: 18287213]

22. Muro S, Mateescu M, Gajewski C, Robinson M, Muzykantov VR, Koval M. Control of intracellular trafficking of ICAM-1-targeted nanocarriers by endothelial Na<sup>+</sup>/H<sup>+</sup> exchanger proteins. *Am J Physiol Lung Cell Mol Physiol* 2006;290:L809–L817. [PubMed: 16299052]
23. Kozower BD, Christofidou-Solomidou M, Sweitzer TD, Muro S, Buerk DG, Solomides CC, et al. Immunotargeting of catalase to the pulmonary endothelium alleviates oxidative stress and reduces acute lung transplantation injury. *Nat Biotechnol* 2003;21:392–398. [PubMed: 12652312]
24. Shuvaev VV, Christofidou-Solomidou M, Scherpereel A, Simone E, Arguiri E, Tliba S, et al. Factors modulating the delivery and effect of enzymatic cargo conjugated with antibodies targeted to the pulmonary endothelium. *J Control Release* 2007;118:235–244. [PubMed: 17270308]
25. Muro S, Cui X, Gajewski C, Murciano JC, Muzykantov VR, Koval M. Slow intracellular trafficking of catalase nanoparticles targeted to ICAM-1 protects endothelial cells from oxidative stress. *Am J Physiol Cell Physiol* 2003;285:C1339–C1347. [PubMed: 12878488]
26. Schuchman, EH.; Muro, S. The development of enzyme replacement therapy for lysosomal diseases: Gaucher disease and beyond. In: Futerman, AH., editor. *Gaucher Disease: Lessons Learned About Therapy of Lysosomal Disorders*. Vol. 1. CRC; Boca Raton: 2006. p. 125-140.
27. Koval M, Preiter K, Adles C, Stahl PD, Steinberg TH. Size of IgG-opsonized particles determines macrophage response during internalization. *Exp Cell Res* 1998;242:265–273. [PubMed: 9665824]
28. Champion JA, Mitragotri S. Role of target geometry in phagocytosis. *Proc Natl Acad Sci USA* 2006;103:4930–4934. [PubMed: 16549762]
29. Muro S, Koval M, Muzykantov V. Endothelial endocytic pathways: gates for vascular drug delivery. *Curr Vasc Pharmacol* 2004;2:281–299. [PubMed: 15320826]
30. Stan RV. Endocytosis pathways in endothelium: how many? *Am J Physiol Lung Cell Mol Physiol* 2006;290:L806–L808. [PubMed: 16603594]
31. Schuchman, EH.; Desnick, RJ. Niemann-Pick disease types A and B: acid sphingomyelinase deficiencies. In: Scriver, C.; Beaudet, A.; Sly, W.; Valle, D.; Childs, B.; Kinzler, K., et al., editors. *The Metabolic and molecular Bases of Inherited Disease*. Vol. 8. McGraw-Hill; New York: 2001. p. 3589-3610.
32. He X, Miranda SR, Xiong X, Dagan A, Gatt S, Schuchman EH. Characterization of human acid sphingomyelinase purified from the media of overexpressing Chinese hamster ovary cells. *Biochim Biophys Acta* 1999;1432:251–264. [PubMed: 10407147]
33. Li S, Nickels J, Palmer AF. Liposome-encapsulated actin-hemoglobin (LEAcHb) artificial blood substitutes. *Biomaterials* 2005;26:3759–3769. [PubMed: 15621266]
34. Geng Y, Cai S, Tsai R, Tewari M, Minko T, Discher DE. Shape effects of filaments versus spherical particles in flow and drug delivery. *Nat Nanotech* 2007;2:249–255.
35. Oh P, Borgstrom P, Witkiewicz H, Li Y, Borgstrom BJ, Chrastina A, et al. Live dynamic imaging of caveolae pumping targeted antibody rapidly and specifically across endothelium in the lung. *Nat Biotechnol* 2007;25:327–337. [PubMed: 17334358]
36. Garnacho C, Shuvaev V, Thomas A, McKenna L, Sun J, Koval M, et al. RhoA activation and actin reorganization involved in endothelial CAM-mediated endocytosis of anti-PECAM carriers: critical role for tyrosine 686 in the cytoplasmic tail of PECAM-1. *Blood* 2008;111:3024–3033. [PubMed: 18182571]
37. Minshall RD, Sessa WC, Stan RV, Anderson RG, Malik AB. Caveolin regulation of endothelial function. *Am J Physiol Lung Cell Mol Physiol* 2003;285:L1179–L1183. [PubMed: 14604847]
38. Rejman J, Oberle V, Zuhorn IS, Hoekstra D. Size-dependent internalization of particles via the pathways of clathrin- and caveolae-mediated endocytosis. *Biochem J* 2004;377:159–169. [PubMed: 14505488]
39. Hillebrand U, Hausberg M, Stock C, Shahin V, Nikova D, Riethmuller C, et al. 17beta-estradiol increases volume, apical surface and elasticity of human endothelium mediated by Na<sup>+</sup>/H<sup>+</sup> exchange. *Cardiovasc Res* 2006;69:916–924. [PubMed: 16412402]
40. Matsusue Y, Hanafusa S, Yamamuro T, Shikinami Y, Ikada Y. Tissue reaction of bioabsorbable ultra high strength poly (L-lactide) rod. A long-term study in rabbits. *Clin Orthop Relat Res* 1995;317:246–253. [PubMed: 7671487]

41. Avgoustakis K, Beletsi A, Panagi Z, Klepetsanis P, Karydas AG, Ithakissios DS. PLGA-mPEG nanoparticles of cisplatin: *in vitro* nanoparticle degradation, *in vitro* drug release and *in vivo* drug residence in blood properties. *J Control Release* 2002;79:123–135. [PubMed: 11853924]
42. Panyam J, Labhasetwar V. Biodegradable nanoparticles for drug and gene delivery to cells and tissue. *Adv Drug Deliv Rev* 2003;55:329–347. [PubMed: 12628320]

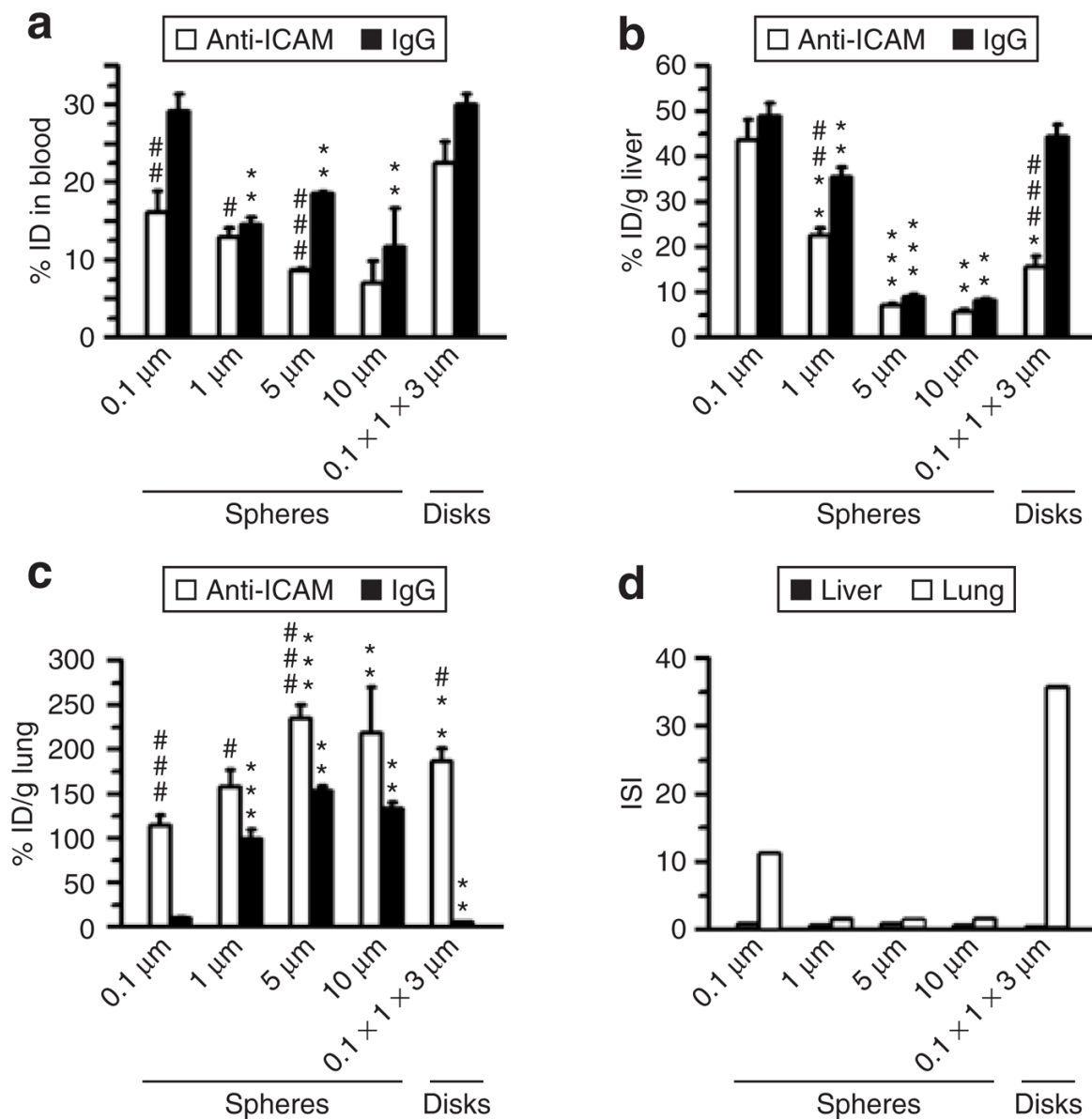


**Figure 1. Role of geometry in the pharmacokinetics and biodistribution of anti-ICAM carriers in mice**

(a) Blood level of anti-ICAM (white bars) versus immunoglobulin G (IgG) (black bars) particles of various geometries (0.1, 1, 5, and 10  $\mu\text{m}$  spheres, and 0.1  $\times$  1  $\times$  3  $\mu\text{m}$  disks), calculated as percentage of injected dose (% ID) remaining in the circulation 1 minute after intravenous injection in C57BL/6 mice. (b) Liver uptake and (c) lung uptake (expressed as % ID per gram) of anti-ICAM (white bars) versus IgG (black bars) formulations, 30 minutes after injection. (d) The immunospesificity index (ISI) in liver (black bars) and lung (white bars) represents the anti-ICAM-to-IgG particle ratio, calculated as % ID/g in each of these tissues. Data are mean  $\pm$  SEM ( $n \geq 4$  mice). \*, Compares particles of any given micron-range size to 0.1  $\mu\text{m}$ . #, compares anti-ICAM particles to IgG counterparts. \* or #,  $P \leq 0.05$ ; \*\* or ##,  $P \leq 0.01$ ; \*\*\* or ###,  $P \leq 0.001$ , by Student's  $t$ -test. ICAM, intercellular adhesion molecule 1.

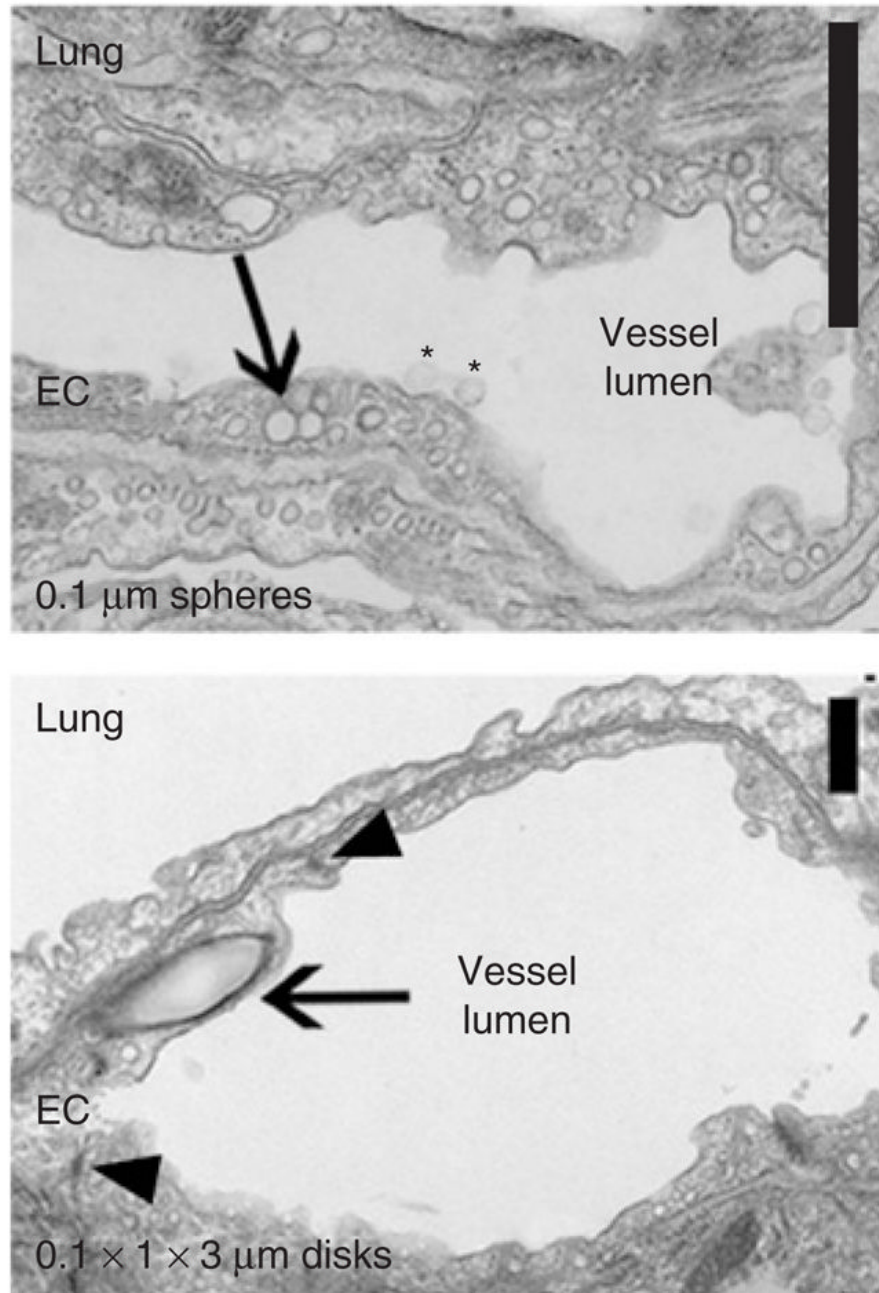


**Figure 2. Internalization of anti-ICAM carriers by endothelial cells (ECs) *in vivo***  
 Transmission electron microscopy micrographs showing binding (asterisks) and internalization (arrows) of 0.1- $\mu\text{m}$  anti-ICAM/spheres and 0.1  $\times$  1  $\times$  3  $\mu\text{m}$  anti-ICAM/disks by pulmonary ECs 3 hours after injection. Intact cell junctions are marked by arrowheads. Scale bar = 1  $\mu\text{m}$ . ICAM, intercellular-adhesion molecule 1.

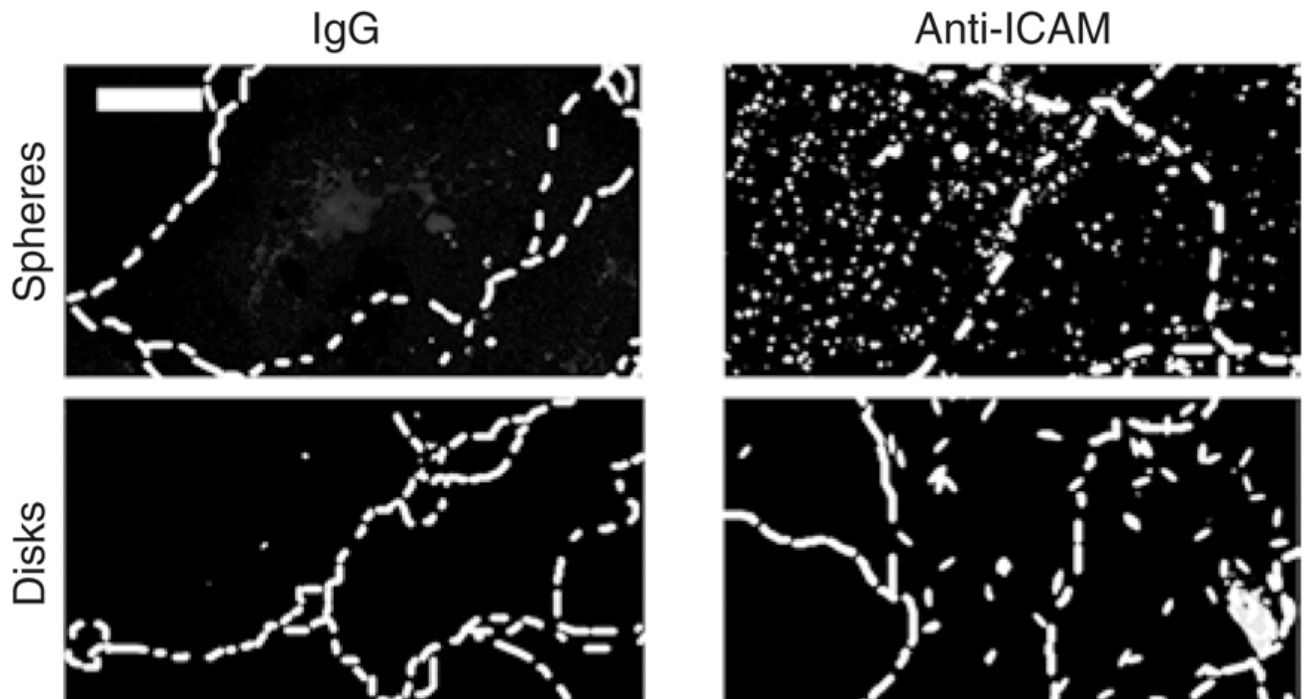


**Figure 3. Specific binding of anti-ICAM carriers to endothelial cells in culture**

As an example, the fluorescent images show specific binding of fluorescein isothiocyanate–labeled 0.1- $\mu\text{m}$  anti-ICAM spheres and  $0.1 \times 1 \times 3 \mu\text{m}$  anti-ICAM disks versus immunoglobulin G (IgG) counterparts to tumor necrosis factor- $\alpha$  activated HUVECs (30 minutes incubation at 4 °C). Scale bar = 10  $\mu\text{m}$ . The cells borders have been marked by a dashed line from phase-contrast images. ICAM, intercellular-adhesion molecule 1.

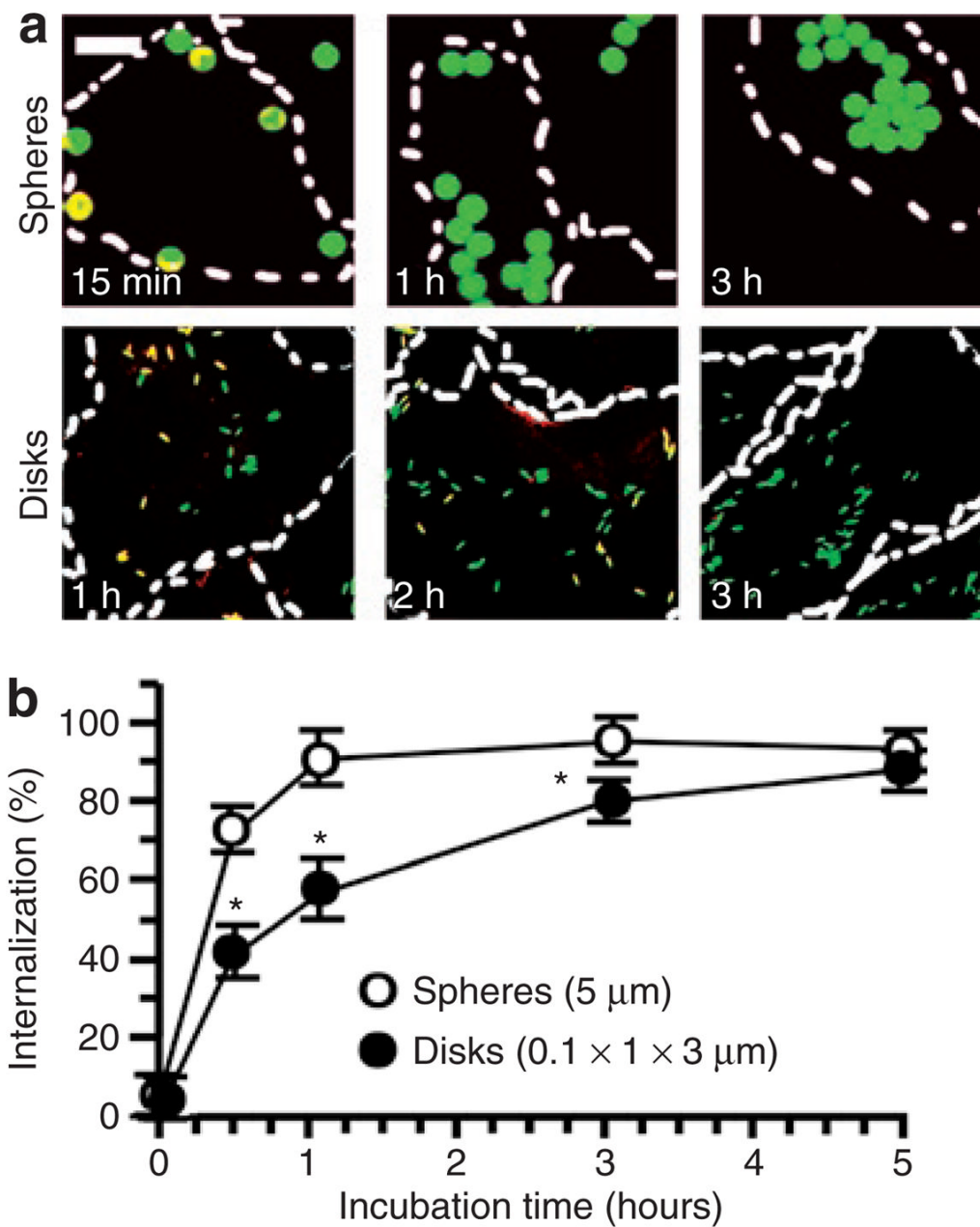


**Figure 4. Role of geometry in the endocytosis of anti-ICAM carriers by endothelial cells**  
**(a)** Fluorescence micrographs showing internalized fluorescein isothiocyanate-labeled (green) anti-ICAM/spheres (5 μm diameter) versus anti-ICAM/disks (0.1 × 1 × 3 μm) incubated with tumor necrosis factor-α activated HUVECs at 37 °C for the indicated time. Counterstaining with a Texas red secondary antibody reveals surface-accessible anti-ICAM particles (yellow). Dashed line = cell borders determined from phase-contrast images of cell monolayers. Scale bar = 10 μm. **(b)** Comparison of internalization kinetics of these anti-ICAM particle formulations, automatically quantified from fluorescence micrographs. Data are mean ± SEM ( $n \geq 25$  cells, two experiments). \*Compares spheres to elliptical disks at any given time point. \*,  $P \leq 0.05$ , by Student's  $t$ -test. ICAM, intercellular-adhesion molecule 1.

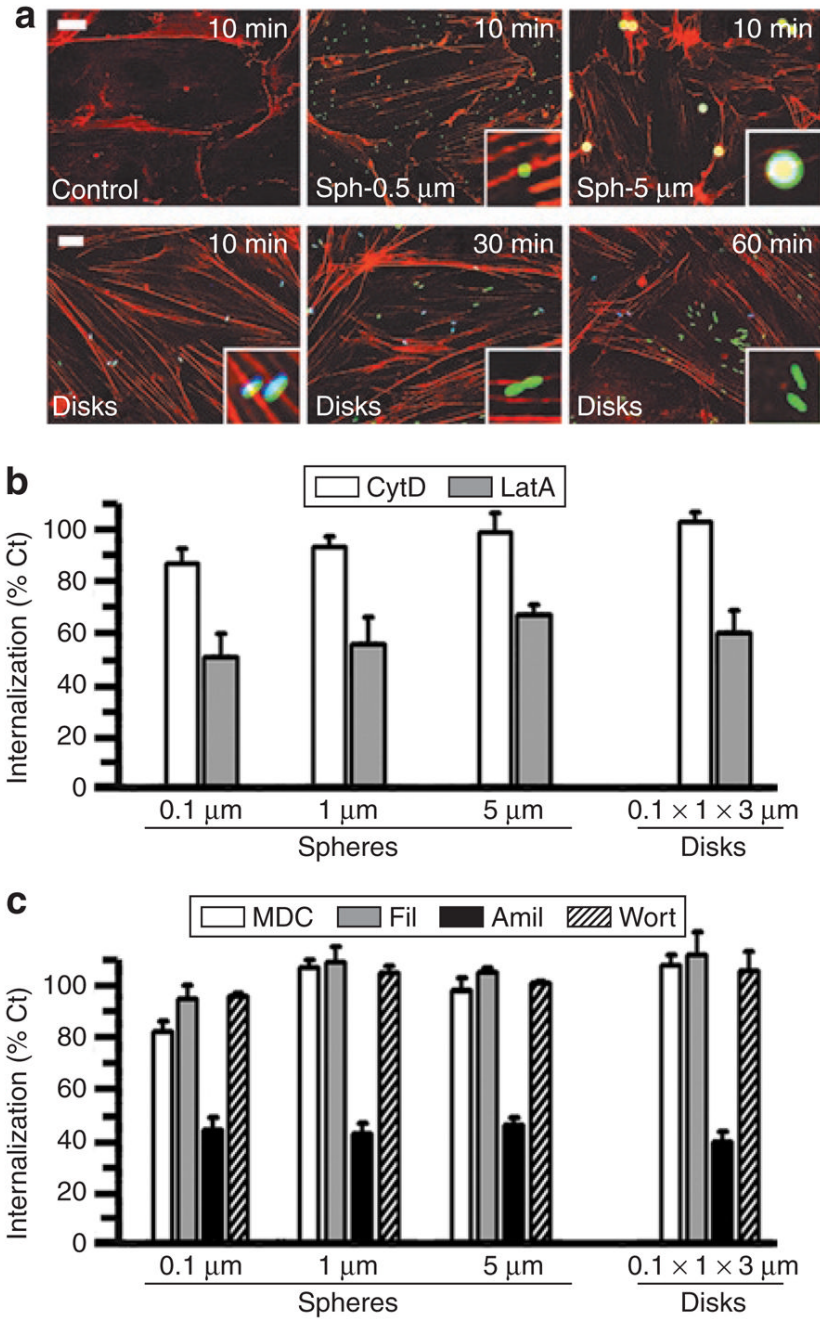


**Figure 5. Mechanism of endocytosis of anti-ICAM carriers of various geometries**

(a) Fluorescence microscopy showing formation of actin stress fibers (stained by red Alexa Fluor 594 phalloidin) upon incubation of activated HUVECs with fluorescein isothiocyanate-labeled anti-ICAM/spheres (0.5 and 5 μm diameter) or anti-ICAM/disks (0.1 × 1 × 3 μm) for the indicated time. Particles in the cell surface look blue due to counter-staining with blue Alexa Fluor 350 goat anti-mouse immunoglobulin G. Scale bar = 10 μm. (b) Internalization (1 hour) of anti-ICAM spherical particles of various sizes (0.1, 1, and 5 μm diameter) and elliptical disks (0.1 × 1 × 3 μm) in the presence of two pharmacological inhibitors of actin filaments (0.5 μmol/l cytochalasin D or CytD, and 0.1 μmol/l latrunculin A or LatA). (c) The effects of pharmacological inhibitors of clathrin-coated pits (50 μmol/l monodansyl

cadaverine, MDC), caveolar-mediated endocytosis (1  $\mu\text{g/ml}$  filipin, Fil), a common inhibitor to macropinocytosis and CAM endocytosis (3  $\text{mmol/l}$  amiloride, Amil), and a macropinocytosis inhibitor (0.5  $\mu\text{mol/l}$  Wortmannin, Wort), were tested as in **(b)**. Data are mean  $\pm$  SEM ( $n \geq 25$  cells, two experiments). Calculated with respect to control cells (%Ct). ICAM, intercellular adhesion molecule 1.

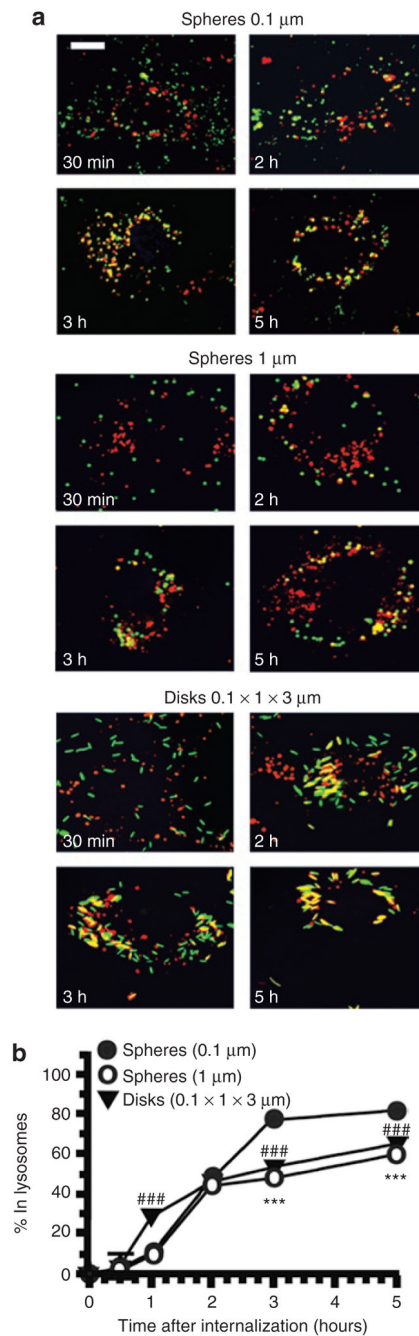


**Figure 6. Role of geometry on the intracellular trafficking of anti-ICAM carriers**

(a) Fluorescence micrographs showing trafficking of fluorescein isothiocyanate–labeled (green) anti-ICAM carriers of various geometries (0.1 and 1  $\mu\text{m}$  spheres, and 0.1  $\times$  1  $\times$  3  $\mu\text{m}$  disks) to Texas red dextran prelabeled lysosomes (red). Lysosomal colocalization is visualized as yellow. Scale bar = 10  $\mu\text{m}$ . (b) Trafficking of anti-ICAM carriers to lysosomes was calculated as percent colocalization of these fluorescent markers determined by microscopy at the indicated time. Data are mean  $\pm$  SEM ( $n > 25$  cells, two experiments). Low-value error bars are masked by symbols in the graph. \*, Compares 1  $\mu\text{m}$  spheres to 0.1  $\mu\text{m}$  particles at any given time point. #, compares 0.1  $\times$  1  $\times$  3  $\mu\text{m}$  disks to 0.1  $\mu\text{m}$  particles at any given time point.

\* or #,  $P \leq 0.05$ ; \*\* or ##,  $P \leq 0.01$ ; \*\*\* or ###,  $P \leq 0.001$ , by Student's *t*-test. ICAM, intercellular-adhesion molecule 1.

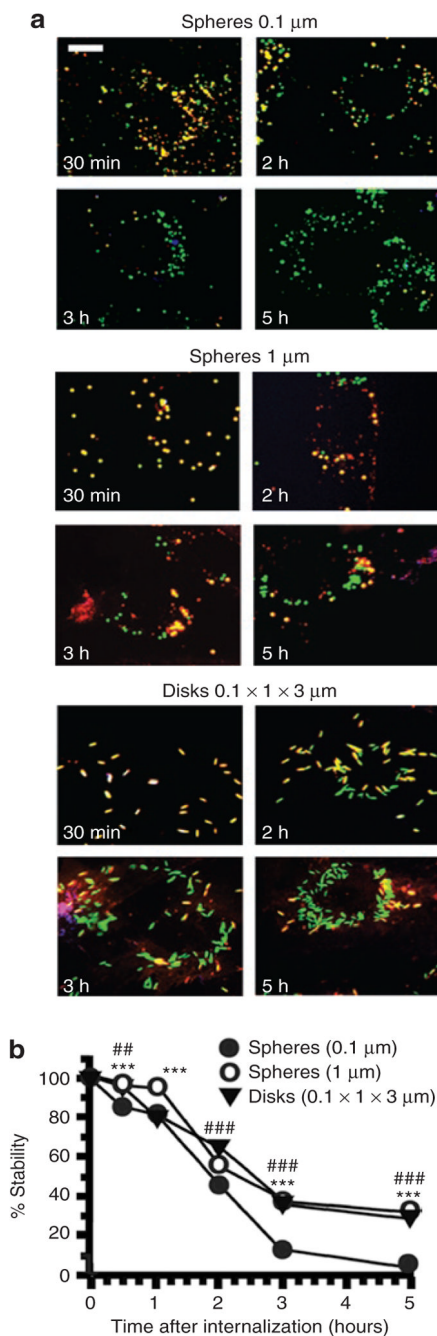


**Figure 7. Role of geometry on the intracellular stability of anti-ICAM carriers**

(a) Fluorescence micrographs showing fluorescein isothiocyanate-labeled (green) anti-ICAM carriers of various geometries (0.1 and 1  $\mu\text{m}$  spheres, and 0.1  $\times$  1  $\times$  3  $\mu\text{m}$  disks), after counterstaining surface-bound carriers with a blue Alexa Fluor 350 secondary antibody to anti-ICAM. The stability of anti-ICAM protein counterpart in the internalized carrier (green) was then assessed by anti-ICAM immunodetection using a Texas red-conjugated secondary antibody after cell permeabilization. Hence, yellow denotes stability of anti-ICAM carrier counterpart. Scale bar = 10  $\mu\text{m}$ . (b) Proteolytic degradation of anti-ICAM protein counterpart onto the particles quantified from fluorescence micrographs. Data are mean  $\pm$  SEM ( $n > 25$  cells, two experiments). Low-value error bars are masked by symbols in the graph. \*, compares

1  $\mu\text{m}$  spheres to 0.1  $\mu\text{m}$  particles at any given time point. #, Compares  $0.1 \times 1 \times 3 \mu\text{m}$  disks to 0.1  $\mu\text{m}$  particles at any given time point. \* or #,  $P \leq 0.05$ ; \*\* or ##,  $P \leq 0.01$ ; \*\*\* or ###,  $P \leq 0.001$ , by Student's *t*-test. ICAM, intercellular-adhesion molecule 1.

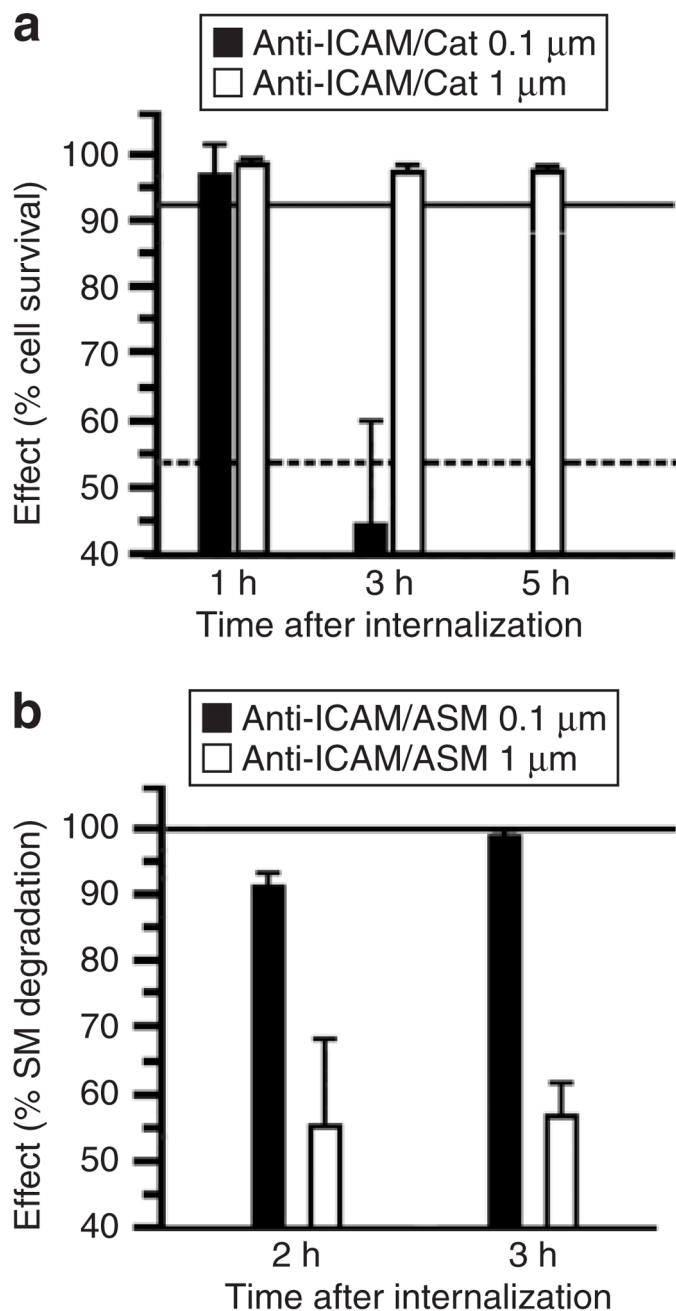


**Figure 8. Role of geometry on the functional therapeutic activity of anti-ICAM carriers**  
**(a)** Induction of oxidative injury in HUVECs with 5 mmol/l H<sub>2</sub>O<sub>2</sub> after delivery of antioxidant catalase by 0.1 versus 1 μm spherical anti-ICAM particles. Cell survival was estimated by labeling HUVECs with Live/Dead assay and fluorescent imaging. Data are mean ± SEM ( $n \geq 500$  cells/condition). The continuous and dashed lines in the graph represent survival levels of noninjured cells and H<sub>2</sub>O<sub>2</sub>-treated cells, respectively, tested after incubation with control 0.1 μm anti-ICAM particles. **(b)** Aberrant storage of sphingomyelin (SM), typical of the lysosomal storage disorder type A and B Niemann–Pick disease, was induced in HUVECs by treatment with 50 μmol/l imipramine. SM was labeled in these deficient cells by incubation for 16 hours at 37 °C with a BODIPY-FL<sub>C12</sub>-SM analog. Reduction of SM within these intracellular

compartments was imaged after internalization of recombinant acid sphingomyelinase, delivered by either 0.1 versus 1  $\mu\text{m}$  spherical anti-ICAM carriers. Intracellular level of SM was quantified by fluorescence microscopy, and normalized to SM levels in normal HUVECs versus diseased HUVECs before enzyme replacement. Data are mean  $\pm$  SEM ( $n \geq 10$  cells, two assays). ICAM, intercellular-adhesion molecule 1.